Comparative assessment of continuum-scale models of bimolecular reactive transport in porous media under pre-asymptotic conditions

by G.M. Porta[1], G. Ceriotti[1] and J.-F. Thovert[2]

[1]Dipartimento di Ingegneria Civile ed Ambientale, Politecnico di Milano, Piazza L. Da Vinci 32,
20133 Milano, Italy
[2]Institut Pprime, CNRS, SP2MI, BP 30179, 86962 Futuroscope Cedex, France

ABSTRACT

We compare the ability of various continuum-scale models to reproduce the key features of a transport setting associated with a bimolecular reaction taking place in the fluid phase and numerically simulated at the pore-scale level in a disordered porous medium. We start by considering a continuum-scale formulation which results from formal upscaling of this reactive transport process by means of volume averaging. The resulting (upscaled) continuum-scale system of equations includes nonlocal integro-differential terms and the effective parameters embedded in the model are quantified directly through computed pore-scale fluid velocity and pore space geometry attributes. The results obtained through this predictive model formulation are then compared against those provided by available effective continuum models which require calibration through parameter estimation. Our analysis considers two models recently proposed in the literature which are designed to embed incomplete mixing arising from the presence of fast reactions under advection dominated transport conditions. We show that best estimates of the parameters of these two models heavily depend on the type of data employed for model calibration. Our upscaled nonlocal formulation enables us to reproduce most of the critical features observed through pore-scale simulation without any model calibration. As such, our results clearly show that embedding into a continuum-scale model the information content associated with pore-scale geometrical features and fluid velocity yields improved interpretation of typically available continuum-scale transport observations.

Keywords: reactive transport; continuum-scale models; upscaling; parameter estimation; pore-scale modeling

1. INTRODUCTION

Recent developments in pore-scale numerical modeling and imaging technologies are providing remarkable added value to our knowledge of dynamics of reactive transport processes in complex pore spaces (e.g., *Molins et al.*, 2014; *Menke et al.*, 2015). These techniques and approaches allow characterizing and comparing the relative importance of the dynamics associated with advective transport, diffusive mixing and reactive processes at the (micron) scale of individual pores. Reactive transport applications in hydrogeology typically involve large spatial scales. It would then be desirable to explore the extent at which our knowledge on pore-scale dynamics could be transferred into models that can be applied at a continuum- (or Darcy-) scale. In this work we consider solute transport in porous media in the presence of a homogeneous bimolecular irreversible reaction of the kind A + B → C, which is typically classified as a fluid-fluid reaction. Upscaling this reactive transport problem from the pore- to a continuum-scale is especially challenging under conditions of advection dominated transport and fast reaction, respectively associated with large values of the Péclet, *Pe*, and Damköhler, *Da*, numbers (e.g. *Gramling et al.,* 2002; *Tartakovsky et al.*, 2009; *Porta et al.*, 2012a). Available column experiments at the laboratory scale document the space-time dynamics of the reaction product C (*Gramling et al.,* 2002; *Raje and Kapoor*, 2000). These works show that the assumption of complete mixing of the reactants at the pore-scale can lead to considerable discrepancies between measured concentration of the reaction product C and predictions based on continuum-scale approximations. This result is consistent with theoretical upscaling by *Battiato and Tartakovsky* (2011). Experimental observations documenting the evolution of the pore-scale reaction rate in a Hele-Shaw cell are illustrated by *de Anna et al.* (2013, 2014). These authors show that the spatial distribution of the reaction rates within the pore space is highly non uniform in space and is characterized by a filamentary structure. The pore-scale dynamics of the process of mixing of the reactants, which is inherently linked to the reaction product, has also been investigated through detailed numerical simulations in various settings (e.g., *Tartakovsky et al.,* 2009; *Willingham et al.,* 2010; *Porta et al.* 2012b, 2013; *Hochstetler and Kitanidis,* 2013; *Rolle and Kitanidis*, 2014; *Alhashmi et al.*, 2015). These studies emphasize the critical importance of a proper model of local mixing for the interpretation of reactive transport processes. Similar conclusions are drawn from column scale experiments where pH-controlled reactions take place (e.g., *Jose and Cirpka*, 2004; *Loyaux-Lawniczak et al.*, 2012; *Edery et al.*, 2015).

Several alternative approaches have been proposed with the aim of embedding effects of pore-scale incomplete mixing within Darcy-scale effective reactive transport models (see also the review by *Edery et al.*, 2013). These include particle-based Lagrangian methodologies (e.g., *Edery et al.* 2009, 2010; *Ding et al.*, 2013) as well as Eulerian approaches (e.g., *Sanchez-Vila et al.*, 2010; *Chiogna and Bellin*, 2013; *Hochstetler and Kitanidis*, 2013). Here we focus on the latter set of approaches as applied to bimolecular fluid-fluid reactions. Continuum-scale approaches typically embed effective formulations, which encode incomplete mixing effects into transport and reaction parameters. These effective formulations typically require model calibration against a set of observations, and can be used to interpret available data. In this context, a series of works (e.g., *Sanchez-Vila et al.*, 2010; *Chiogna and Bellin*, 2013; *Rubio et al.*, 2008) are focused on the interpretation of the experimental dataset of *Gramling et al.* (2002). These authors document the spatial distribution of the reaction product concentration within a fully saturated column where the host porous medium is a bead pack. Longitudinal (i.e., along the mean flow direction of flow) profiles of solute concentration are reported for diverse time levels and transport conditions. A comparison of the results obtained in the above referenced works shows that very different modeling approaches allow interpreting this particular experimental dataset with comparable levels of accuracy. This suggests that the information content associated with the distribution of the reaction product in the system is insufficient for a unique characterization of incomplete mixing through effective continuum-scale approaches. *Alhashmi et al.* (2015) perform a three-dimensional pore-scale simulation in an attempt to replicate the reactive experiment scenario of *Gramling et al.* (2002). They show that spreading of the reactants across the medium can be quantified in terms of a time dependent dispersion coefficient. The temporal evolution of longitudinal spreading is different for the two reactants A and B. However, to the best of our knowledge, the ability of effective models to characterize the concentration of the two reactants (A and B) within the regions where they mix and the reactive process takes place has not been tested to date.

A mathematical formulation relating pore-scale characteristics and effective reactive transport parameters at a continuum-scale can be derived through formal upscaling methodologies, such as the method of volume averaging (e.g., *Whitaker*, 1999; *Orgogozo et al.*, 2010; *Valdes-Parada et al*., 2011; *Guo et al.*, 2015). The latter is applied to bimolecular reactive transport by *Porta et al.* (2012a). These authors show that it is possible to obtain a closed nonlocal formulation of a reaction term associated with incomplete mixing in the presence of of a fast reaction (i.e., large *Da* values). The assumptions underlying the theoretical analysis of *Porta et al.* (2012a) have been verified by comparison against direct numerical upscaling of pore-scale simulations performed in simple two-dimensional geometries, i.e., a plane channel (*Porta et al.*, 2012b) and an ordered array of cylinders (*Porta et al.*, 2013). The continuum-scale model proposed by *Porta et al.* (2012a) is presented in terms of a nonlocal integro-differential formulation, consistent with a recent formulation obtained by *Hansen et al.* (2014) starting from the generalized master equation. Note that the formulation proposed by *Porta et al.* (2012) accounts for the temporal dynamics of the spreading process discussed by *Alhashmi et al.* (2015) by including a nonlocal in time dispersive transport term.

In this work we start from pore-scale numerical simulations of a bimolecular homogeneous and fast reaction. We consider the latter to take place within a two-dimensional pore space, which is generated by randomly placing in space a set of circular grains of uniform diameter. The key target of the work is to test our ability to interpret the continuum-scale results obtained from direct upscaling of pore-scale simulations in such a disordered system through continuum-scale models. The reactive transport setting we analyze is similar to the one considered, e.g., in *Gramling et al.* (2002), and we model it in terms of an effective one-dimensional unsteady transport process at the continuum-scale. We distinguish two different approaches, depending on the type of information employed to compute the associated model parameters: (1) an approach based on the use of effective models which require calibration against reactive transport features that are typically observed at the continuum scale, e.g., spatial distribution or breakthrough curves of reactants; and (2) an approach based on upscaled models which only require information on pore-space geometry and on the velocity field to predict reactive transport at the continuum-scale.

A first goal of this work is to provide the numerical approximation of the nonlocal upscaled model of bimolecular reactive transport derived by *Porta et al.* (2012a). We then consider three additional effective reactive transport models, i.e., the typical advection dispersion reaction equation, which implicitly assumes complete mixing at pore-scale, and the models proposed by *Sanchez-Vila et al.* (2010) and *Hochstetler and Kitanidis* (2013). These models differ in terms of the formulation employed to characterize the effective reaction parameters. Consistent with typical applications, we estimate these parameters through results obtained from numerical upscaling of pore-scale calculations.

Available experimental datasets typically document the evolution of the reaction product in space and time (*Gramling et al.*, 2002; *Raje and Kapoor*, 2000). Therefore, the majority of previous works dealing with this reactive transport setting are solely based on the interpretation of the space-time evolution of the reaction product. In this work we explicitly consider the model performance also in terms of its ability to capture the dynamics of the concentrations of the two reactants A and B. This aspect is key in a pre-asymptotic transport regime, where the characterization of transport can be significantly affected by the initial distribution of the reactants in the domain (e.g., *Alhashmi et al.*, 2015). We compare the ability of all these model formulations to interpret the considered reactive transport process and analyze the impact of incorporating diverse types of information in the estimation of model parameters. By doing so, we also identify the critical relevance of specific formats assumed by continuum-scale reactive and transport terms. The results of this work allow quantifying the relevance of nonlocal terms in the reactive transport setting we analyze.

The work is organized as follows. Section 2 provides a description of the pore-scale problem setting. Section 3 is devoted to a presentation of the continuum-scale modeling options we implement. In Section 4 we assess the capabilities of the selected continuum-scale models to interpret the pore-scale simulation results. Concluding remarks end the work.

2. PROBLEM SETTING

We consider the two-dimensional domain Ω filled by a fully saturated porous medium, consisting of a liquid (Ω_l) and a solid fraction (Ω_s). The porous domain is constituted by a collection of periodic unit cells, Ω'. The geometry of the unit cell is generated by the disordered superposition of circular grains of uniform diameter $\hat{w} = 0.08$ mm and is characterized by a porosity $\phi \approx 0.6$ (see Figure 1). Note that here and in the following all primed variables are defined within a unit cell and hat-signed variables are dimensional. The liquid and the solid phases share an impermeable boundary surface, Γ_{ls}. Fluid flow through the pore space is associated with a steady laminar two-dimensional velocity field, $\hat{\mathbf{u}}(\hat{\mathbf{x}})$, which satisfies the Stokes problem. The flow field is driven by a unit pressure gradient along the *x*-direction and a zero pressure gradient along the *y*-direction (Figure 1). The numerical approximation of the velocity field is obtained by the methodology introduced by *Bekri et al*. (1995) and *Coelho et al.* (1997). A desired value of average fluid velocity, $\hat{U}$, along the *x*-direction is imposed by multiplying the computed velocity field by an appropriate constant. Figure 1 depicts the dimensionless velocity norm $|\mathbf{u}| = |\hat{\mathbf{u}}| / \hat{U}$. We observe velocity values which are smaller than $\hat{U}$ (i.e., $|\mathbf{u}| < 1$) throughout most of the domain, values of $|\mathbf{u}|$ > 3 being mostly concentrated only within a few pore throats. One can clearly identify the presence of regions which are characterized by small velocity values and are poorly connected to the flow preferential path (e.g., regions highlighted in Figure 1). The dimensionless velocities varies in space over a range of values which is comparable to that obtained by flow simulation performed within millimeter-scale imaged rock samples (see e.g., *Bijeljic et al.*, 2013).

The external boundary Γ_{ext} of Ω_l can be subdivided into three parts according to the sign of $\hat{\mathbf{u}}(\hat{\mathbf{x}}) \cdot \mathbf{n}_e$, i.e., Γ_{in} ($\hat{\mathbf{u}}(\hat{\mathbf{x}}) \cdot \mathbf{n}_e > 0$), Γ_{out} ($\hat{\mathbf{u}}(\hat{\mathbf{x}}) \cdot \mathbf{n}_e < 0$), and Γ_{imp} ($\hat{\mathbf{u}}(\hat{\mathbf{x}}) \cdot \mathbf{n}_e = 0$), $\mathbf{n}_e$ being the inward unit vector normal to the boundary. A bimolecular irreversible reaction of the kind A + B

→ C takes place in the liquid phase and it is assumed not to affect the velocity field and the pore space geometry. Molecular diffusion is modeled through the standard Fick's law. We employ the following dimensionless formulation of the reactive transport problem (*Porta et al.*, 2013)

$$\frac{\partial c_i}{\partial t} + \mathbf{u} \cdot \nabla c_i = \frac{1}{Pe} \nabla^2 c_i \qquad i = D, E \qquad (1)$$

$$\frac{\partial c_B}{\partial t} + \mathbf{u} \cdot \nabla c_B = \frac{1}{Pe} \nabla^2 c_B - \frac{Da}{Pe} c_B (c_B - c_D) \qquad (2)$$

where

$$\hat{c}_i = \hat{c}_0 c_i \,,\; \hat{\mathbf{u}} = \hat{U} \mathbf{u} \,,\; \hat{t} = t \frac{\hat{\ell}}{\hat{U}} \,,\; \hat{\nabla} = \frac{\nabla}{\hat{\ell}} \,,\; Pe = \frac{\hat{U} \hat{\ell}}{\hat{D}_m} \,,\; Da = \frac{\hat{k} \hat{c}_0 \hat{\ell}^2}{\hat{D}_m} \qquad (3)$$

$\hat{c}_i$ is concentration, $\hat{c}_0$ is a reference concentration; $\hat{k}$ [m^3/(mol s)] is the reaction kinetic constant; $\hat{D}_m$ is molecular diffusion $\hat{\ell}$ is a characteristic spatial dimension; and *Pe* and *Da* are the Péclet and Damköhler numbers, respectively. Note that (1)-(2) are written in terms of the conservative components $c_D = c_B - c_A$ and $c_E = c_B + c_C$. System (1)-(2) can be readily obtained from algebraic recombination of the mass conservation equations written for the three chemical species A, B and C (e.g., *Porta et al.*, 2012a and references therein).

We consider a replacement setting: the system is initially saturated by a constant concentration $\hat{c}_0$ of species A for $x > 0$; species B is introduced continuously in the system for $t > 0$ at a constant concentration $\hat{c}_0$ through the boundary Γ_{in}. Equations (1)-(2) are then completed by the following boundary and initial conditions

$$\mathbf{n} \cdot \nabla c_i = 0 \qquad i = B, D, E \,; \qquad \mathbf{x} \in \Gamma_{ls}, \Gamma_{imp}, \Gamma_{out} \qquad (4)$$

$$\mathbf{u} \cdot \mathbf{n}_e c_i(\mathbf{x}, t) + \frac{1}{Pe} \mathbf{n}_e \cdot \nabla c_i(\mathbf{x}, t) = N_i \,,\; i = B, D, E \qquad \mathbf{x} \in \Gamma_{in} \qquad (5)$$

$$c_B(\mathbf{x},0)=0,\ c_D(\mathbf{x},0)=-1,\ c_E(\mathbf{x},0)=0 \qquad \mathbf{x}\in\Omega_l, x>0 \tag{6}$$

$$c_B(\mathbf{x},0)=1,\ c_D(\mathbf{x},0)=1,\ c_E(\mathbf{x},0)=1 \qquad \mathbf{x}\in\Omega_l, x<0 \tag{7}$$

A flux boundary conditions is assumed at Γ_{in} so that $c_B = c_D = c_E = 1$. Zero flux is imposed on the liquid-solid interface Γ_{ls}, and Γ_{imp}. Note that the boundary Γ_{in} is located at $x = -60$ so that the pore space is saturated with a constant concentration of B at $t = 0$ within the first unit cell adjacent to the inlet section (i.e., for –60 < x < 0). This choice allows avoiding any influence of the inlet boundary condition on the reactive process at early times.

The reactive transport problem is solved within the pore space by means of the particle tracking methodology described by *Porta et al.* (2012b, 2013) and adapted from routines developed by *Bekri et al.* (1995) and *Debenest et al.* (2005) for the pore scale description of reactive transport. We select $\hat{\ell} = \hat{w} = 0.08$ mm and set *Pe* = 24.88 (i.e., average velocity $\hat{U} = 0.62$ mm/s, Reynolds number *Re* = 0.05) and *Da* = 1038. This value of *Pe* is computed by relying on the average fluid velocity and suggests that the process takes place under moderately advection-dominated conditions. We note that the local velocity distribution displays large variations within the considered disordered cell (see Figure 1). The relative strength of the time scales related to transport by advection and diffusion can be evaluated through the local Péclet number $Pe_{loc}(\mathbf{x}) = |\hat{\mathbf{u}}|\hat{\ell} / \hat{D}_m$ (*Porta et al.*, 2015). One can expect transport to be strongly advection-dominated along the fast channels detected in the system, where the largest values of velocity are about one order of magnitude larger than the average velocity (i.e., $|\mathbf{u}| \approx 10, Pe_{loc}(\mathbf{x}) \approx 250$), while diffusion drives solute transport within the cavities, where the fluid is basically immobile, i.e. $Pe_{loc}(\mathbf{x}) \approx 0$.

The total longitudinal length of the system is L = 1200 ($\hat{L} = 9.6$ cm), i.e. we consider a collection of 20 unit cells Ω' along the x-direction. Our computations rely on a discretization of the pore space into elementary squares K (pixels) of size 0.02 mm. As in *Porta et al.* (2013), we consider a unit concentration to be equivalent to a number of particles $NP_K = 100$ per elementary square. Note that, as a result of these modeling choices, simulating a uniform unit concentration of a single chemical species along the whole computational domain requires a number of approximately 1.7×10^7 particles. This yields reliable local (pixel-scale) concentration values for $c > 5 \times 10^{-3}$ (*Porta et al.*, 2013, 2012b).

Figure 2 shows a snapshot of the spatial distribution of c_A, c_B and c_C within the pore space for t = 448. Note that reactant A is initially residing in the system. Positive values of c_A are observed for x < 500 solely within pores which are scarcely accessible to flow, these areas corresponding to regions (cavities) highlighted in Figure 1. The invading reactant B tends to follow the principal pathways, characterized by large velocity values. As a consequence, local concentrations of reactants exhibit significant and sharp variations across relatively small distances. We also observe that reactant concentrations are anti-correlated, i.e., c_B is small in pores where concentration of A is significant and vice versa, due to the occurrence of the fast reaction. This is consistent with previous computational analyses in regular two-dimensional geometries (*Porta et al.*, 2013). The concentration of the reaction product C in Figure 2 displays a peak value at $x \approx 450$. Contributions to c_C in the forward tail (x > 500) are mainly associated with regions characterized by large velocity, stagnant regions chiefly contributing to the backward tail (x < 400).

Pore-scale simulation results are used in the following as calibration and validation data against which outputs of continuum-scale models are compared. For this purpose we consider section-averaged concentrations in the fluid phase. These are defined as

$$\bar{c}_i\left(x\right) = \frac{1}{H\bar{\eta}}\int_H c_i\left(x,y\right)dy \; ; \qquad \bar{\eta} = \frac{1}{H}\int_H G\left(x,y\right)dy \tag{8}$$

where *H* is the total length of the porous medium along *y*, $\bar{c}_i$ is section-averaged concentration of local concentrations c_i of chemical species *i* = A, B, or C and *G*(*x*,*y*) is an indicator function, i.e. *G*(*x*,*y*) = 0, 1 respectively for solid grains and fluid.

3. CONTINUUM-SCALE MODELS

A number of approaches have been proposed to model this reactive problem at the Darcy-scale. In this work we consider three existing effective models together with the upscaled formulation stemming from volume averaging of the system (1)-(2), as provided by *Porta et al.* (2012a). In Section 3.1 we summarize the salient features of the considered effective models. Section 3.2 recalls the definition of the continuum-scale system resulting from volume averaging of the pore-scale system (1)-(2).

3.1 Effective models

Effective continuum models of reactive transport are typically formulated through an advection dispersion reaction equation (ADRE)

$$\frac{\partial C_i}{\partial t} = \frac{1}{Pe}(D^* + 1)\frac{\partial^2 C_i}{\partial x^2} - U\frac{\partial C_i}{\partial x} \qquad i = D, E \tag{9}$$

$$\frac{\partial C_B}{\partial \hat{t}} = \frac{1}{Pe}\left(D^* + 1\right)\frac{\partial^2 C_B}{\partial x^2} - U\frac{\partial C_B}{\partial x} - K_{eff} C_B\left(C_B - C_D\right) \tag{10}$$

where $D^* = \hat{D}^* / \hat{D}_m$ is the dimensionless longitudinal dispersion coefficient, K_{eff} is an effective reaction constant, C_i (i = B, D, E) are continuum-scale concentrations. We consider in the following three models for K_{eff} proposed in the literature:

- Model 1 (complete mixing):

$$K_{eff} = \frac{Da}{Pe} \tag{11}$$

- Model 2 (*Sanchez Vila et al*., 2010):

$$K_{eff} = \beta \frac{Da}{Pe}; \ \beta = \frac{\hat{\beta}_0 \hat{t}^{-m}}{\hat{k}} \tag{12}$$

  where $\hat{\beta}_0$ and m are parameters to be estimated through model calibration.

- Model 3 (*Hochstetler and Kitanidis,* 2013):

$$K_{eff} = E_F \frac{Da}{Pe}; \ E_F = \frac{\gamma\lambda}{Da + \lambda} \tag{13}$$

  where E_F is the reaction effectiveness factor, γ and λ being model parameters.

Model 1 implies that the same reaction constant can be employed at the pore and continuum-scales, i.e. reactants are assumed to be completely mixed at the pore-scale. Models 2 and 3 account for the effect of incomplete mixing of the reactants through the effective reaction parameters (12)-(13). The definitions in (12)-(13) are motivated by previous literature approaches to model conservative and reactive transport. *Sanchez-Vila et al*. (2010) introduce (12) based on the rate-limited mass transfer process observed by *Haggerty et al.* (2004). *Hochstetler and Kitanidis* (2013) introduce the reaction effectiveness factor E_F (13) following the definition of the segregation intensity introduced by *Kapoor et al.* (1997).

3.2 Upscaled transport model

Porta et al. (2012a) perform an upscaling of (1)-(2) through the volume averaging method (*Whitaker*, 1999). Due to the nature of the scenario we consider, we recall here the corresponding one-dimensional formulation, which is labeled as model 4 in the following. A key target of the volume averaging analysis is to obtain a closure formulation in terms of the intrinsic volume averaged concentration

$$\left\langle c_i \right\rangle^l = \frac{1}{\phi V(\mathbf{x})} \int_V c_i\left(\mathbf{x}\right) dV \tag{14}$$

where $V(\mathbf{x})$ is a volume of porous medium within Ω. The volume averaged formulation for the conservative species reads

$$\frac{\partial \left\langle c_i \right\rangle^l}{\partial t} = -\left\langle u \right\rangle^l \frac{\partial \left\langle c_i \right\rangle^l}{\partial x} + \frac{1}{Pe}\frac{\partial}{\partial x}\left[\left(1 + D_U\right) * \frac{\partial}{\partial t}\left(\frac{\partial \left\langle c_i \right\rangle^l}{\partial x}\right)\right] \quad i = D, E \tag{15}$$

where

$$D_U * \frac{\partial}{\partial t}\left(\frac{\partial \left\langle c_i \right\rangle^l}{\partial x}\right) = \int_0^t D_U\left(t - \tau\right) \frac{\partial}{\partial \tau} \frac{\partial \left\langle c_i \right\rangle^l}{\partial x} d\tau \, ; \qquad D_U = \frac{1}{V}\int_{V_{ls}} b n_x dA + \left\langle \tilde{u} b \right\rangle^l \tag{16}$$

is the dispersion coefficient, $\tilde{u} = u - \left\langle u \right\rangle^l$ is a spatial fluctuation (or deviation) of the velocity in the *x*-direction within the pore space, and *b* is a closure variable. Equations (15)-(16) are based on the following unsteady closure relationship (*Moyne*, 1997; *Chastanet and Wood*, 2008)

$$\tilde{c}_i = c_i - \left\langle c_i \right\rangle^l = b\left(\mathbf{x}', t\right) * \frac{\partial}{\partial t} \frac{\partial \left\langle c_i \right\rangle^l}{\partial x} \tag{17}$$

where $\tilde{c}_i = c_i - \langle c_i \rangle^l$ (i = D,E) is a spatial fluctuation of the concentration about the mean. The medium we consider is characterized by a periodic structure and the closure variable *b* can be computed within a unit cell. The following differential problem is satisfied by *b*

$$\frac{\partial b}{\partial t} + \left(\mathbf{u} \nabla b + \tilde{u} \right) = \frac{1}{Pe} \nabla^2 b \qquad \mathbf{x}' \in \Omega_l', t > 0 \tag{18}$$

$$\mathbf{n} \cdot \nabla b = n_x \qquad \mathbf{x}' \in \Gamma_{ls}', t > 0 \tag{19}$$

$$b\left(\mathbf{x}', 0 \right) = 0 \qquad \mathbf{x}' \in \Omega_l', t = 0 \tag{20}$$

Here, we have considered the unit cell reference system $\mathbf{x}'$, with the corresponding liquid Ω_l' domain and the liquid-solid surface Γ_{ls}'. The format of the transport equation for the reactive species B depends on the relative importance of *Da* as compared to *Pe*. Here, we consider *Da* >> *Pe* so that (*Porta et al.*, 2012a)

$$\frac{\partial \langle c_B \rangle^l}{\partial t} + \langle u \rangle^l \frac{\partial \langle c_B \rangle^l}{\partial x} = \frac{1}{Pe} \frac{\partial}{\partial x} \left[\frac{\partial \langle c_B \rangle^l}{\partial x} + M \left(D_U - 1 \right) * \frac{\partial}{\partial t} \left(\frac{\partial \langle c_D \rangle^l}{\partial x} \right) \right] - \frac{Da}{Pe} \left(R_1 + R_2 \right) \tag{21}$$

where

$$R_1 = \langle c_B \rangle^l \left(\langle c_B \rangle^l - \langle c_D \rangle^l \right) \tag{22}$$

$$R_2 = M \left(M - 1 \right) \left\langle \left(b * \frac{\partial}{\partial t} \frac{\partial \langle c_D \rangle^l}{\partial x} \right)^2 \right\rangle_l \tag{23}$$

and $M = \dfrac{\langle c_B \rangle^l}{\langle c_B \rangle^l + \langle c_A \rangle^l} = \dfrac{\langle c_B \rangle^l}{2\langle c_B \rangle^l - \langle c_D \rangle^l}$. The reaction terms (22)-(23) stem from volume averaging of the pore-scale reaction term

$$\left\langle c_B \left(c_B - c_D \right) \right\rangle^l \approx \langle c_B \rangle^l \left(\langle c_B \rangle^l - \langle c_D \rangle^l \right) + \left\langle \tilde{c}_B \left(\tilde{c}_B - \tilde{c}_D \right) \right\rangle^l \tag{24}$$

Porta et al. (2012a) propose the following closure approximation for *Da* >> *Pe*

$$\tilde{c}_B \approx \tilde{c}_D \frac{\langle c_B \rangle^l}{2\langle c_B \rangle^l - \langle c_D \rangle^l} = M\tilde{c}_D = Mb * \frac{\partial}{\partial t}\frac{\partial \langle c_D \rangle^l}{\partial x} \tag{25}$$

Substitution of (25) in (24) leads to $R_2 \approx \left\langle \tilde{c}_B \left(\tilde{c}_B - \tilde{c}_D \right) \right\rangle^l$. We refer to the formulation (15)-(21) as model 4 in Section 4 for simplicity. The parameters appearing in (15)-(21) can be fully characterized from pore-scale geometry and velocity distribution upon solving the system (18)-(20). We do so by implementing a finite element formulation of (18)-(20) in the FreeFEM++ environment (*Hecht et al*., 2012). We discretize the solution in space through a stabilized streamline diffusion finite element formulation while employing a first order implicit backward Euler finite difference scheme in time. We compute the solution by employing a structured grid formed by approximately 10^5 triangular elements.

Figure 3 depicts the time evolution of the coefficients D_U (16) and of the quantity

$$B_2(t) = \left\langle b(\mathbf{x}', t)^2 \right\rangle_l \tag{26}$$

We select B_2 as a measure of the nonlocal reaction term (23), i.e., the localized counterpart of (23) reads

$$R_{2,LOC} = M(M-1)B_2(t)\left(\frac{\partial \langle c_D \rangle^l}{\partial x} \right)^2 \tag{27}$$

We observe that both D_U and B_2 vary over a wide range of values and are always increasing within the considered time window. This result evidences that the reactive transport process we observe takes place within a pre-asymptotic regime. Therefore, the nonlocal terms embedded in (15)-(21) can be expected to play a relevant role in the reactive system characterization.

The numerical solution of the upscaled system requires the discretization of the integro-differential terms appearing in (15)-(21). We employ a trapezoid integration rule to discretize the integral terms (16) and (23) in the time domain. System (15)-(21) is approximated through a fixed space and time discretization. We select a time step $\Delta t = 2$ and a spatial discretization step $\Delta x = 1$. We numerically verified through a grid convergence analysis that the results do not depend on the spatial discretization and time step size (details not shown). We also verify that the results of the nonlocal solution reproduce those of the corresponding local formulation when parameters are constant in time. The computational time associated with a run of the nonlocal model 4 is approximately 10^5 s (28 hours) on a processor Intel(R) Pentium(R) III Xeon processor 2.83 GHz. For comparison, note that the numerical solution of the effective models (9)-(10) requires approximately 10^3 s on the same processor.

4. COMPARATIVE ASSESSEMENT OF CONTINUUM-SCALE MODELS

In this section we discuss the ability of the continuum-scale models introduced in Section 3 to reproduce the results obtained by pore-scale simulation of the reactive transport process.

As anticipated in the Introduction, we compare two classes of models which are distinguished on the basis of the information sources employed to characterize the model parameters and are associated with diverse levels of complexity. Models 1-3 have a simple structure, but their effective parameters are estimated through model calibration, i.e. they incorporate information on the output concentration profiles. On the other hand, model 4 is characterized by a complex structure, and the related parameters are estimated relying solely on pore-scale information, i.e. no model calibration is required. Our model comparison aims at assessing the impact of the critical differences amongst the considered continuum-scale models on the ability of the models to reproduce our pore-scale reference solution. These key differences can be classified as illustrated in the following. With reference to transport, model 4 is nonlocal in time and allows accounting for non-Fickian dispersion effects, as opposed to models 1-3 which are all based on an assumed Fickian dispersion process. With reference to the way reaction is embedded in the model, model 4 entails a space and time dependent nonlocal formulation of the reaction rate constant; model 2 embeds a time dependent effective reaction parameter K_{eff} through (12); while models 1 and 3 employ a constant effective reaction coefficient, K_{eff} .

In the following, we start by discussing the characterization of the parameters of models 1-3, which is performed through calibration against concentration profiles extracted from the reference pore-scale simulation. We then compare the results of the set of the four continuum-scale models illustrated in Section 3 against (section-averaged) pore-scale simulation results.

4.1 Calibration of the effective models

The characterization of the effective models (9)-(13) (models 1-3) is here performed through the estimation of the embedded effective parameters, performed via model calibration. The model calibration parameters we consider are listed in Table 1 for each of the three models.

The longitudinal dispersion coefficient is considered as a calibration parameter for all three models. This choice is motivated from results of previous studies focusing on the interpretation of the dataset of *Gramling et al.* (2002). In this context, *Alhashmi et al.* (2015) demonstrate through numerical pore-scale simulation that transport in the system is still in a pre-asymptotic stage. Otherwise, results by *Sanchez-Vila et al.* (2010) show that a Fickian model can be employed to interpret the same reactive transport dataset up to a reasonable accuracy by including the dispersion coefficient as a parameter to be estimated through model calibration against the reactive transport data.

Models 2 and 3 both embed two additional calibration parameters which are associated with the respective reaction models, i.e. $\hat{\beta}_0$ and *m* in (12) for model 2, γ and λ in (13) for model 3. Given the structure of the reactive term in (13), we note that infinite combinations of γ, λ can lead to the same effective reaction constant for a given *Da*. This implies that joint estimation of γ and λ is possible only when calibration data associated with diverse values of *Da* are available. Since we consider here a unique value of *Da*, we follow the indication of *Hochstetler and Kitanidis* (2013) and set $\gamma = 1$ while estimating λ.

Our aim is here to study the performance of these models in the presence of different sets of calibration data. We consider two sets of such data, i.e., concentration profiles of the invading reactant B (dataset $\overline{c}_{Bi}^{*}$) and of the reaction product C (dataset $\overline{c}_{Ci}^{*}$) at a fixed dimensionless time, ($t = 448$). We select this time level because it is the longest time considered in the pore-scale simulation. We then calibrate all three models by employing separately the two datasets. Entries of the calibration datasets are concentrations $\overline{c}_{Bi}^{*}$ ($i = 1 \ldots N_{DB}$), and $\overline{c}_{Ci}^{*}$ ($i = 1 \ldots N_{DC}$), N_{DB} and N_{DC} indicating the number of data included in the datasets $\overline{c}_{Bi}^{*}$ and $\overline{c}_{Ci}^{*}$, respectively. We select values $\overline{c}_{Ci}^{*}$ as

$$\overline{c}_{Ci}^{*} = \frac{1}{L'} \int_{L' \cdot (i-1)}^{L' \cdot i} \overline{c}_C dx \qquad i = 1, \ldots, 20 \qquad (28)$$

where $L' = 60$ is the length of the unit cell Ω' along the *x*-direction. In other words, we consider the 20 unit cells constituting the total length *L* of the porous domain and identify $\overline{c}_{Ci}^{*}$ as the spatial average of the pore-scale concentrations of the reaction product c_C computed within each of the unit cells (i.e, we set $N_{DC} = 20$).

Entries of dataset $\overline{c}^{*}_{Bi}$ are selected in a similar way, i.e., as the spatial average of the concentration in the liquid phase

$$\overline{c}^{*}_{Bi} = \frac{1}{L'}\int_{L'\cdot(i-1)}^{L'\cdot i} \overline{c}_B dx \qquad i = 1,\ldots,8 \tag{29}$$

Note that positive values of c_B are observed only for x < 500, i.e., in the first 8 unit cells. We augment the entries in this calibration dataset by considering additional concentration values at locations close to the reaction front ($x \approx 450$), because one of our goals is the characterization of the parameters of the incomplete mixing models which are expected to influence concentration values at such locations. As such, dataset $\overline{c}^{*}_{Bi}$ includes a total of 16 data which are distributed along the length of the porous domain ($N_{DB} = 16$). The spatial distributions of the calibration data $\overline{c}^{*}_{Bi}$ and $\overline{c}^{*}_{Ci}$ are depicted in Figure 4a and 4d, respectively.

Model parameters are estimated either through the datasets $\overline{c}^{*}_{Bi}$ or $\overline{c}^{*}_{Ci}$ by considering the following metrics

$$J_C = \frac{1}{N_{DC}}\sum_{i=1}^{N_{DC}}\left[\overline{c}^{*}_{Ci} - C_C\left(x_i\right)\right]^2 \tag{30}$$

$$J_B = \frac{1}{N_{DB}}\sum_{i=1}^{N_{DB}}\left[\overline{c}^{*}_{Bi} - C_B\left(x_i\right)\right]^2 \tag{31}$$

where $C_J\left(x_i\right)$ (J = B, C) is the continuum-scale model output at location x_i corresponding to the location of data $\overline{c}^{*}_{Bi}, \overline{c}^{*}_{Ci}$. We employ criteria (30)-(31) in a maximum likelihood framework (*Carrera and Neuman*, 1986), where we assume the covariance matrix associated with measurements error to be equal to a diagonal matrix with constant entries. This enables us to compute the covariance matrix of the estimation error

$$\mathbf{Q}_{k,C_j} = \sigma^2_{k,C_j}\left(\mathbf{J}^T_{k,C_j}\mathbf{J}_{k,C_j}\right)^{-1} \qquad k = 1, 2, 3;\ j = B, C \qquad (32)$$

where indices k and j respectively indicate the model and the dataset employed for model calibration, $\sigma^2_{k,C_j} = J_{j,min} / N_{Dj}$ is the estimated model error, $\mathbf{J}_{k,j}$ is the Jacobian matrix whose entries are the derivatives of the output state variables C_j with respect to the parameters of model k. The diagonal entries of matrix (32) quantify the uncertainty σ^2_p associated with the ML estimate of model parameter p.

Table 1 lists the values of the estimated parameters and the related standard deviation σ_p, together with the minimum values of (30)-(31) (respectively denoted as J_{Cmin} and J_{Bmin}) obtained through calibration against the two types of data $\overline{c}^*_{Bi}$ and $\overline{c}^*_{Ci}$ for each of the three effective models (9)-(13). The calibrated model results are compared in Figure 4 against the calibration data and the complete profile of section-averaged concentrations $\overline{c}_B(x)$ and $\overline{c}_C(x)$ rendered by pore-scale simulation at $t = 448$. Models 2 and 3 lead to smaller values of J_{Cmin} than model 1. This result is consistent with previous analysis (*Sanchez-Vila et al.*, 2010; *Hochstetler and Kitanidis*, 2013) and supports the idea that effective models 2-3 can interpret the distribution of the reaction product in the reactive transport setting we analyze in the presence of pore-scale incomplete mixing of reactants. We also observe that the values of J_{Bmin} are similar for models 1 and 2 and J_{Bmin} is largest for model 3. We note that values of standard deviation σ_p associated with the estimates of the dispersion parameters are about 5-10 % of the corresponding ML estimate for all three models and for the two considered datasets, thus resulting in relatively small coefficients of variation. These results suggest that the data convey appropriate information to characterize the longitudinal dispersion coefficients. However, note that the estimated longitudinal dispersion coefficients are significantly different across models and/or depending on the type pf calibration data employed. Model calibrations based solely on $\overline{c}_{Bi}^{*}$ yield estimated longitudinal dispersions which are considerably larger than those based on $\overline{c}_{Ci}^{*}$ (see Table 1). This leads to an increased spreading of the reaction product when these models are calibrated against $\overline{c}_{Bi}^{*}$ as opposed to what can be obtained by employing $\overline{c}_{Ci}^{*}$ as a calibration dataset (see Figure 4b and d).

The estimate of parameter m in model 2 rendered by calibration against $\overline{c}_{Ci}^{*}$ is consistent with the value obtained by *Sanchez-Vila et al.* (2010) by using the same type of information. Note that Table 1 lists $\hat{\beta}_0$ in dimensional units [$\mathrm{m}^3\mathrm{mol}^{-1}\mathrm{s}^{m-1}$]. Given that the dimensional units of this parameter depend on the specific value assumed by the exponent m, the values of $\hat{\beta}_0$ obtained in Table 1 are hardly comparable to those obtained in *Sanchez-Vila et al.* (2010). The best estimate obtained for parameter λ in model 3 is of the same order of magnitude of the one obtained by *Hochstestler and Kitanidis* (2013) when $\overline{c}_{Ci}^{*}$ data are employed. In general, we observe that the estimated values of the effective reaction parameters embedded in models 2 and 3 largely depend on the type of information available for calibration.

Figure 4d shows that the peak of concentration C_C rendered by models 2 and 3 is smaller than that associated with model 1 when $\overline{c}_{Ci}^{*}$ is considered for calibration. Otherwise, the three effective models yield the same concentration peak of C_C when their parameters are estimated against $\overline{c}_{Bi}^{*}$ (see Figure 4b). Previous studies (e.g., *Sanchez-Vila et al.*, 2010; *Chiogna and Bellin*, 2014) show that the evolution of the peak concentration is typically linked to incomplete mixing of the reactant at pore-scale. We further note from Table 1 that the standard deviations related to the effective reaction parameters embedded in models 2 (i.e, $\hat{\beta}_0$ and m) and 3 (i.e, λ) are much larger when calibration is performed through dataset $\overline{c}^*_{Bi}$ than by relying on $\overline{c}^*_{Ci}$. Therefore, results in Figure 4b and 4d and Table 1 suggest that an accurate estimation of the incomplete mixing parameters embedded in models 2 and 3 requires information on the reaction product concentration. This result can be explained upon observing that the output concentration C_B rendered by the investigated continuum models attains very small values close to the reaction front. Large variations of the incomplete mixing parameters induce modest variations of C_B. Otherwise, the peak concentration of C_C is very sensitive to variations of these reaction model parameters, as previously shown by *Sanchez-Vila et al.* (2010), *Chiogna and Bellin* (2013), and *Ciriello et al.* (2015). Therefore, model calibration against $\overline{c}^*_{Ci}$ yields a reduced uncertainty for the reaction parameters which represent incomplete mixing, as compared to results obtained through calibration based on $\overline{c}^*_{Bi}$ observations.

4.2 Model comparison

In this Section we aim at assessing the performance of the diverse effective and upscaled models in reproducing the pore-scale simulation results, which represent our reference solution.

We compare in our discussion the results obtained through calibration of the effective models 1-3 against the dataset $\overline{c}^*_{Ci}$ (see Section 4.1) and the prediction yielded by model 4 on the basis of pore-scale information. We focus on a comparison of the longitudinal profiles of concentrations of the three chemical species as rendered by pore- and continuum-scale models and quantify model performance through some global indicators.

Figures 5a-f depict a comparison between the concentration profiles rendered by the numerical solution of the continuum-scale models and section-averaged concentration obtained through the pore-scale simulation for solutes A (Figure 5a-b), B (Figure 5c-d) and C (Figure 5e-4f) at two selected (dimensionless) times, i.e., $t = 74$ (Figure 5a,c,e) and $t = 448$ (Figure 5b,d,f). As time advances, B displaces A and the two reactants mainly mix in a limited region around the the interface between B and A (i.e., the reaction front), which migrates in the system by advection. Owing to our choice of dimensionless space-time reference, the reaction front is found at locations $x \approx t$ for each considered time level. The backward tail of $\overline{c}_A$ in our reference pore-scale solution displays an oscillatory behavior characterized by isolated localized peaks (see Figures 5a-b, respectively for $x < 70$, $x < 400$). These oscillations are related to the investigated pore structure, i.e. they are chiefly due to the presence of cavities in the porous domain where the solute is trapped for long times (see also Figures 1-2). As time progresses, the reaction front advances in the porous domain by advection and new immobile (or low velocity) zones with $\overline{c}_A > 0$ remain isolated and surrounded by the invading solute B (see Figure 2). Thus, the number of localized concentration peaks in the profile of $\overline{c}_A$ increases with time. The effect of these low-velocity zones is also detected on $\overline{c}_B$ and $\overline{c}_C$ profiles (Figures 5c-d and e-f). The section-averaged concentrations of reactants B and A show an anti-correlated behavior, i.e. sharp increases of A concentrations correspond to localized declines of B concentrations, consistent with the pore-scale spatial distributions depicted in Figure 2. The presence of cavities (poorly connected and almost immobile zones) results in localized high concentration peaks that are also visible in the profiles of the reaction product C, which is delayed in low velocity regions. We note that this phenomenon is not observed when considering experimental measurements and numerical simulation of the same reactive process within three-dimensional regular porous media, e.g., glass beads packing (*Gramling et al.*, 2002; *Alhashmi et al.*, 2015). The considered disordered two-dimensional porous medium includes poorly connected and essentially stagnant regions, giving rise to the local accumulations of species A and C observed in Figure 5.

All continuum-scale models considered in this study fail to reproduce trapping of concentration of species A within immobile regions (see Figure 5b). To quantify the relevance of this inaccuracy, we consider the temporal evolution of RC_A, the residual average concentration of A, in a subregion of our computational domain

$$RC_A(t) = \frac{1}{X_M} \int_0^{X_M} C_A(x,t)\, dx \qquad (33)$$

$X_M < L$ identifying the longitudinal size of a given subdomain we consider. The time evolution of RC_A enables us to evaluate the residence time of reactant A in the system. As an example, Figure 6a depicts the evolution of RC_A when $X_M = 300$, i.e. we compute RC_A within a domain segment of longitudinal length corresponding to five unit cells. Since we expect the reaction front to approach the location X_M for $t = X_M$, selecting $X_M = 300$ enables us to characterize the temporal dynamics of RC_A before and after the main reaction front breaks through location X_M within the time window considered in our pore-scale simulation. We observe that the pore-scale simulation yields what appears to be a two-stage evolution of the residual mass of A. This feature is identified by a remarkable change in the slope of $RC_A(t)$ which takes place at $t \approx 300$, i.e. for $t \approx X_M$. For $t < 300$, the average concentration of A progressively decreases to a value approximately equal to 10^{-2}. For $t > 300$, the concentration of A decreases at a lower rate as compared to the above mentioned first stage. In this second stage, the residual mass of A can be found within system cavities and smoothly decreases in time due to reaction. We observe that all four continuum-scale models reproduce almost exactly the (section-averaged) pore-scale results up to a time $t \approx 250$, the evolution of RC_A in the second stage ($t > 300$) being misrepresented by all investigated continuum-scale models. Results in Figure 5a-b and 6a suggest that considering (*a*) effective reaction terms which model incomplete mixing effects (as in models 2-3) and (*b*) time nonlocalities in both transport and reaction terms (as in model 4) has virtually no effect in improving our ability to reproduce the delayed mass of the reactant A within poorly connected cavities. Figure 6a suggests that all four considered continuum-scale models allow reproducing the residual concentration of the reactant A in the system with comparable accuracy, i.e. up to values of 0.03-0.05 (3-5% of the initial concentration of A).

The reference longitudinal profiles of the concentration of the invading reactant, $\overline{c}_B$, are well predicted by model 4 for both considered time levels (see Figure 5c-d). The effective models 1-3 yield $C_B = 1$ for $x < 200$ and $t = 448$, the solution associated with model 4 tending smoothly to unity at $x = 0$ and closely following the trend of the pore-scale results (see Figure 5d). Insets in Figure 5c-d depict profiles of the concentration of the B reactant in semi logarithmic scale. Model 4 reproduces closely the forward tail of the invading reactant, which is mostly affected by the reactive process. Values of $\overline{c}_B$ at locations where $\overline{c}_B < 0.1$ are overestimated by models 2-3 and underestimated by model 1. This result suggests that the volume averaged formulation (15)-(21) (i.e., model 4) leads to an improved continuum-scale representation of mixing at the reactive front, as compared to models 2 and 3, which however provide a reasonably accurate interpretation of the spatial distribution of the concentration of the reaction product C (see Figure 3d).

We consider now the flux weighted concentration of the invading reactant B, corresponding to the solute breakthrough curve (*BTC_B*). The latter is defined as $BTC_B\left(t\right)=C_B\left(X_M,t\right)$ for continuum-scale models and as

$$BTC_B\left(t\right)=\frac{\int_H c_B u dy}{\int_H u dy} \tag{34}$$

when calculations are performed from pore-scale data. Figure 6b depicts the temporal evolution of the breakthrough curve (BTC_B) of B at position $x = X_M = 300$. We observe that model 4 reproduces the pore-scale results more closely than the remaining three effective models. This result is consistent with longitudinal concentration profiles in Figure 5c-d. The observed differences amongst the models can be explained by considering that model 4 accounts for non-Fickian transport through the nonlocal term (16), while models 1-3 consider a Fickian dispersion model. Moreover, the volume-averaged (upscaled) reaction term (22)-(23) renders an improved representation of the mixing of the reactants close to the reactive front as compared to the effective reaction terms embedded in models 2 and 3. This is suggested by the close agreement between the results rendered by model 4 and their pore-scale counterparts for low concentration values. As a consequence, Figure 6b shows that, contrary to the results given by the effective models 1-3, consideration of nonlocal transport effects and of the upscaled reactive terms improves our ability to accurately quantify the arrival times of a reactive solute B at a given location in the system.

Figure 5e-f depicts the comparison between the longitudinal profiles of concentration of the reaction product C rendered by the different models and the reference pore-scale solution. These results are complemented by the temporal evolution of the spatial moments of the reaction product concentration profiles (Figure 7). Figure 7a shows the temporal evolution of the total mass of C in the systems, i.e., the zero order moment of the concentration profile

$$M_{0C}\left(t\right)=\int_L C_C(x,t)dx \tag{35}$$

Figure 7b-c display the evolution of the spreading

$$\sigma_C\left(t\right)=\sqrt{\frac{\int_L C_C\left(x,t\right)\left(x-x_C\right)^2 dx}{M_{0C}}}; \qquad x_C\left(t\right)=\frac{\int_L C_C(x,t)x\,dx}{M_{0C}} \tag{36}$$

and of the skewness

$$\gamma_C\left(t\right)=\int_L C_C\left(x,t\right)\left(\frac{x-x_C\left(t\right)}{\sigma_C\left(t\right)}\right)^3 dx \tag{37}$$

of the concentration of the reaction product. For the pore-scale simulation, quantities (35)-(37) are computed by replacing $C_C\left(x,t\right)$ in the corresponding expression with the section-averaged concentration $\bar{c}_C\left(x,t\right)$.

Figure 7a reveals that effective models 1-3 lead to an overestimation of the total mass of C for early times. These three models yield modest errors for long times (*t* > 300). This is consistent with the observation that the parameters of models 1-3 are estimated through the concentration of C at *t* = 448. Model 4 reproduces accurately the total mass of C for early times, while leading to a slight underestimation of the reference result for *t* > 200. All four continuum-scale models underestimate the total reaction product by less than 10% at time *t* = 448.

Figure 7b depicts the temporal evolution of the spreading of the reaction product C, as quantified through (36), and shows that the longitudinal spreading of the pore-scale concentration c_C is underestimated by about 20% when considering models 1-3, model 4 underestimating it only by 10%. Comparison of the longitudinal profiles reveals that the inaccuracy associated with model 4 is due to an underestimation of spreading in the forward tail (see Figure 5f, $x > 450$). This may be explained by (*i*) the modeling error embedded in the approximations underlying the volume averaging procedure, and (*ii*) numerical inaccuracies related to the approximation of the closure problem (18)-(20) and of the integro-differential terms appearing in (15)-(21). With reference to the latter point, we note that while in this work we implement a standard numerical solver, the development of more sophisticated techniques for the treatment of integro-differential terms might improve the global performance of model 4. A detailed analysis of this aspect is beyond the scope of this contribution. The effective models 1-3 underestimate spreading and do not provide a satisfactory interpretation of delayed concentrations of the reaction product C, even as these are explicitly considered in the model calibration procedure (see Figure 5f).

Pore-scale results display some early time oscillations of the skewness coefficient (Figure 7c). The latter attains a maximum value of 0.05 at $t = 50$. After this time the value of γ_C associated with pore-scale concentration shows a sustained decrease until it attains negative values for $t > 100$. This result is consistent with the asymmetric pattern observed in Figure 5e-f. In particular, Figure 5f shows that for $t = 448$ the backward tail ($x > 450$) is characterized by a smaller average (spatial) gradient than the forward one ($x < 450$). The continuum models 1-3 yield a positive value of γ_C within the whole considered time window. The non-negligible positive value of the skewness observed at early times for models 1-3 is due to the prescribed set of initial and boundary conditions. We observe that γ_C tends to zero for long times when we consider the effective models 1-3, i.e. the spatial distribution of C_C tends to become symmetric around the peak, consistent with the structure of the implied Fickian dispersion picture (see also Figure 5f). Otherwise, results of the nonlocal model 4 are characterized by a negative skewness within most of the considered observation time frame. Even as model 4 underestimates the values of γ_C rendered by pore-scale simulation, it allows capturing the left tailed behavior of C_C . This result is associated with the two features which distinguish model 4 with respect to the effective models 1-3, i.e., (*i*) the nonlocal nature of the embedded dispersive transport term, and (*ii*) the dependence of the reaction term on space and time.

Results of Figure 7 suggest that considering a non-Fickian dispersion model is critical to capture the evolution in time of spreading and of the asymmetry displayed by the longitudinal distribution of the reaction product . This result is consistent with the findings of *Edery et al.* (2009, 2010) and *Alhashmi et al.* (2015). We note that Figure 7a suggests that models based on a Fickian model assumption can interpret the time evolution of the total reaction product mass (corresponding to M_{0C}) with a reasonable accuracy, even under a pre-asymptotic transport regime, as previously shown by *Sanchez-Vila et al.* (2010).

Finally, we observe that models 2, 3 and 4 predict very similar peak values of C_C at t = 448 (Figure 5e-f), in spite of the very different structure exhibited by the reaction terms in the three models. This is a remarkable result, also considering that previous studies identify the peak concentration of C as a key indicator of incomplete mixing in the considered setting (e.g., *Chiogna and Bellin,* 2013; *Sanchez-Vila et al.*, 2010). We emphasize that the profiles associated with models 2 and 3 are obtained through calibration against data of $\overline{c}_C^*$ (see Figure 5f) while model 4 leads to a very similar result directly embedding available information on pore-scale geometry and velocity field, i.e. without the need for any adjustable parameter. The reaction product concentration profile rendered by model 4 shows a change in concavity in the vicinity of the concentration peak for short times (see, e.g., Figure 5e, related to $x \approx 70$). This behavior is likely due to the numerical discretization of the integro-differential terms of the model. This observation is also supported by considering that this feature vanishes for long times (see Figure 5f).

5. CONCLUSIONS

We consider an irreversible homogeneous reaction taking place in a two-dimensional disordered porous medium where pore-scale geometry and velocity are known and study the reactive transport regime characterized by $Da \gg Pe \gg 1$, corresponding to a fast reaction taking place under advection dominated conditions. We simulate the reactive transport process at pore-scale and we consider the pore-scale numerical results as calibration and validation data for continuum-scale models.

We consider three effective models already presented in the literature which require calibration against observed concentration profiles. Our results show that estimates of effective reaction parameters describing incomplete mixing can be remarkably sensitive to the type of concentrations one employs for model calibration, i.e., parameter estimates can be different depending on whether the concentration of the reaction product or of one of the two reactants is employed. This suggests that none of these models include a robust description of the way the totality of pore-scale processes are transferred to continuum-scale formulations in the porous medium we investigate. The estimated parameter values which model the effect of incomplete mixing in the reaction term are characterized by large uncertainty when we employ the concentration of the injected reactant for model calibration. This result suggests that information on concentration of the reaction product is required for a reliable (continuum-scale) characterization of incomplete mixing in the considered setting.

We numerically solve a continuum-scale nonlocal model resulting from an upscaling of the reactive transport setting considered via volume averaging. This model allows predicting the longitudinal distribution of the reactants and of the reaction product without the need of any adjustable parameter, solely requiring available information on pore-scale geometry and velocity. This model is computationally intensive, as compared to the remaining three effective models we analyze, but allows interpreting specific features observed from direct averaging of the pore-scale numerical solution, such as the non-Fickian transport behavior of the invading reactant B and the asymmetric shape of the reaction product concentration profile.

The considered two-dimensional porous system is characterized by a geometry which includes large cavities where the reactant A, initially residing in the system, is trapped for long times. All considered continuum-scale models fail to reproduce residual (normalized) concentrations of A in the system below values of about 3-5%. As a consequence, they are not able to capture the details of the system behavior at large residence times associated with the presence of minute values of trapped mass of solute A. It might be possible that the use of double- or multi-continuum formulations of this reactive transport setting lead to improved interpretation of this specific feature. This aspect will be investigated in future contributions.

ACKNOWLEDGMENT

The financial support of the MIUR Project PRIN 2010/2011 “Hydroelectric energy by osmosis in coastal areas” is gratefully acknowledged. We acknowledge the contribution of Sergey Chaynikov to the pore-scale numerical simulations.

REFERENCES

Alhashmi Z, Blunt BJ, Bijeljic B. Predictions of dynamic changes in reaction rates as a consequence of incomplete mixing using pore-scale reactive transport modeling on images of porous media. J Contam Hydrol 2015; doi: 10.1016/j.jconhyd.2015.06.004.

Battiato I, Tartakovsky DM. Applicability regimes for macroscopic models of reactive transport in porous media. J Contam Hydrol 2011;120–1:18–26.

Bear J, Cheng A. Modeling groundwater flow and contaminant transport. Springer Science & Business Media; 2010.

Bekri S, Thovert J, Adler P. Dissolution of porous media. Chem Eng Sci 1995;50(17):2765-91.

Bijeljic B, Raeini A, Mostaghimi P, Blunt MJ. Predictions of non-Fickian solute transport in different classes of porous media using direct simulation on pore-scale images. Phys Rev E 2013;87(1):013011.

Carrera J, Neuman SP. Estimation of aquifer parameters under transient and steady state conditions: 1. Maximum likelihood method incorporating prior information, Wat Resour Res. 1986, 22 (2):199-210.

Chastanet J, Wood BD. Mass transfer process in a two-region medium, Water Resour Res. 2008;44, W05413.

Chiogna G, Bellin A. Analytical solution for reactive solute transport considering incomplete mixing within a reference elementary volume. Water Resour Res. 2013;49(5):2589-600.

Ciriello V, Edery Y, Guadagnini A, Berkowitz B. Multimodel framework for characterization of transport in porous media. Water Resour Res. 2015;51(5):3384–3402.

Coelho D, Thovert J, Adler PM. Geometrical and transport properties of random packings of spheres and aspherical particles. Phys Rev E. 1997;55(2):1959-78.

De Anna P, Jimenez-Martinez J, Tabuteau H, Turuban R, Le Borgne T, Derrien M, et al. Mixing and reaction kinetics in porous media: An experimental pore-scale quantification. Environ Sci Technol. 2013;48(1):508-16.

De Anna P, Dentz M, Tartakovsky A, Le Borgne T. The filamentary structure of mixing fronts and its control on reaction kinetics in porous media flows. Geophys Res Lett. 2014;41(13):4586-93.

Debenest G, Mourzenko VV, Thovert J-F. Smouldering in fixed beds of oil shale grains. A three-dimensional microscale numerical model. Combust Theor Model. 2005;9: 113–35.

Ding D, Benson DA, Paster A, Bolster D. Modeling bimolecular reactions and transport in porous media via particle tracking. Adv Water Resour. 2013;53:56-65.

Edery Y, Dror I, Scher H, Berkowitz B. Anomalous reactive transport in porous media: Experiments and modeling. Phys Rev E. 2015;91(5):052130.

Edery Y, Guadagnini A, Scher H, Berkowitz B. Reactive transport in disordered media: Role of fluctuations in interpretation of laboratory experiments. Adv Water Resour 2013;51:86–103.

Edery Y, Scher H, Berkowitz B. Particle tracking model of bimolecular reactive transport in porous media. Water Resour Res. 2010;46(7):W07524.

Edery Y, Scher H, Berkowitz B. Modeling bimolecular reactions and transport in porous media. Geophys Res Lett. 2009;36(2) L02407.

Gramling CM, Harvey CF, Meigs LC. Reactive transport in porous media: A comparison of model prediction with laboratory visualization. Environ Sci Technol. 2002;36(11):2508-14.

Guo J, Quintard M, Laouafa F. Dispersion in Porous Media with Heterogeneous Nonlinear Reactions. Transp Porous Med 2015; in press doi:10.1007/s11242-015-0535-4.

Haggerty R, Harvey CF, von Schwerin CF, Meigs LC. What controls the apparent timescales in aquifers and soils? A comparison of experimental results, Water Resour Res 2004;40:W01510.

Hansen SK, Scher H, Berkowitz B. First-principles derivation of reactive transport modeling parameters for particle tracking and PDE approaches. Adv Water Resour. 2014;66:146-158.

Hecht F. New development in Freefem++, J. Numer. Math. 2012;20(3–4):251–266, doi:10.1515/jnum-2012-0013.

Hochstetler DL, Kitanidis PK. The behavior of effective rate constants for bimolecular reactions in an asymptotic transport regime. J Contam Hydrol. 2013;144(1):88-98.

Jose SC, Cirpka OA. Measurement of mixing-controlled reactive transport in homogeneous porous media and its prediction from conservative tracer test data. Environ Sci Technol. 2004;38(7):2089-2096.

Kapoor V, Gelhar LW, Miralles-Wilhelm F. Bimolecular second-order reactions in spatially varying flows: Segregation induced scale-dependent transformation rates. Water Resour Res 1997;33(4):527–36.

Loyaux-Lawniczak S, Lehmann F, Ackerer P. Acid/base front propagation in saturated porous media: 2D laboratory experiments and modeling. J Contam Hydrol. 2012;138-9:15-21.

Menke HP, Bijeljic B, Andrew MG, Blunt MJ. Dynamic three-dimensional pore-scale imaging of reaction in a carbonate at reservoir conditions. Environ Sci Technol. 2015;49(7):4407-14.

Molins S, Trebotich D, Yang L, Ajo-Franklin JB, Ligocki TJ, Shen C, et al. Pore-scale controls on calcite dissolution rates from flow-through laboratory and numerical experiments. Environ Sci Technol. 2014;48(13):7453-60.

Moyne, C. Two-equation model for a diffusive process in porous media using the volume averaging method with an unsteady-state closure, Adv. Water Resour. 1997;20: 63-76.

Orgogozo L, Golfier F, Buès M, Quintard M. Upscaling of transport processes in porous media with biofilms in non-equilibrium conditions, Adv. Water Resour. 2010;33: 585-600.

Porta GM, Chaynikov S, Thovert J, Riva M, Guadagnini A, Adler PM. Numerical investigation of pore and continuum-scale formulations of bimolecular reactive transport in porous media. Adv Water Resour. 2013;62:243-53.

Porta GM, Riva M, Guadagnini A. Upscaling solute transport in porous media in the presence of an irreversible bimolecular reaction. Adv Water Resour. 2012;35:151-62.

Porta GM, Thovert J, Riva M, Guadagnini A, Adler P. Microscale simulation and numerical upscaling of a reactive flow in a plane channel. Phys Rev E. 2012;86(3):036102.

Porta GM, Bijeljic B, Blunt MJ, Guadagnini A. Continuum-scale characterization of solute transport based on pore-scale velocity distributions. Geophys Res Lett. 2015;42(18):7537-7545.

Raje DS, Kapoor V. Experimental study of bimolecular reaction kinetics in porous media. Environ Sci Technol. 2000;34(7):1234-9.

Rolle M, Kitanidis PK. Effects of compound-specific dilution on transient transport and solute breakthrough: A pore-scale analysis. Adv Water Resour. 2014; 71:186-99.

Rubio A, Zalts A, El Hasi C. Numerical solution of the advection–reaction–diffusion equation at different scales. Environmental Modelling & Software. 2008;23(1):90-5.

Sanchez-Vila X, Fernàndez-Garcia D, Guadagnini A. Interpretation of column experiments of transport of solutes undergoing an irreversible bimolecular reaction using a continuum approximation. Water Resour Res. 2010;46(12).

Valdés-Parada FJ, Aguilar-Madera CG, Álvarez-Ramírez J. On diffusion, dispersion and reaction in porous media. Chem Eng Sci 2011;66: 2177-90. doi:10.1016/j.ces.2011.02.016.

Whitaker S. The method of volume averaging. Springer Science & Business Media; 1998.

Willingham T, Zhang C, Werth CJ, Valocchi AJ, Oostrom M, Wietsma TW. Using dispersivity values to quantify the effects of pore-scale flow focusing on enhanced reaction along a transverse mixing zone. Adv Water Resour. 2010;33(4):525-35.

		Model 1	Model 2			Model 3	
Data		D	D	$\hat{\beta}_0$	M	D	λ
$\overline{c}_B^*$	Best estimate	698	678	0.16	0.08	510	87
	σ_p	50	45	2.23	0.25	46	149
	J_{Bmin}	0.0102	0.0093			0.0194	
$\overline{c}_C^*$	Best estimate	388	423	0.04	0.76	415	2.08
	σ_p	36	56	1.019	0.24	34	1.36
	J_{Cmin}	0.0102	0.0071			0.0071	

Table 1: Results of effective model calibration: best estimate of model parameters, related standard deviation σ_p, as evaluated through the diagonal entries of **Q** (32), and associated minimum values of metrics (30)-(31).

FIGURES

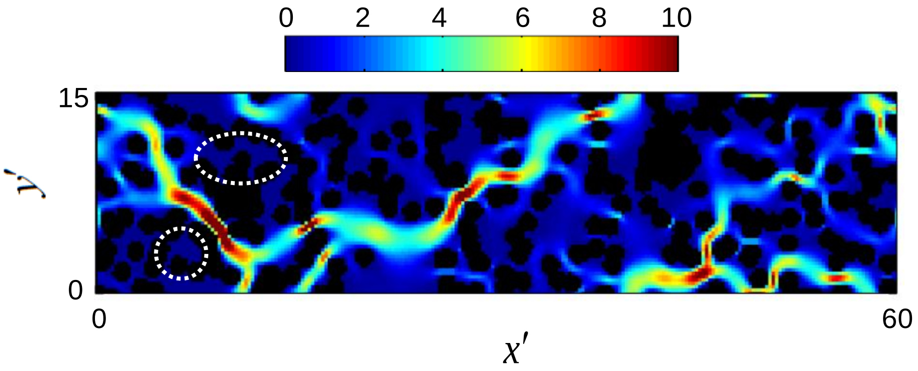

Figure 1. Distribution of velocity $|\mathbf{u}| = |\hat{\mathbf{u}}| / \hat{U}$ within a unit cell Ω'. Areas enclosed by the white dotted circles correspond to cavities characterized by low velocity.

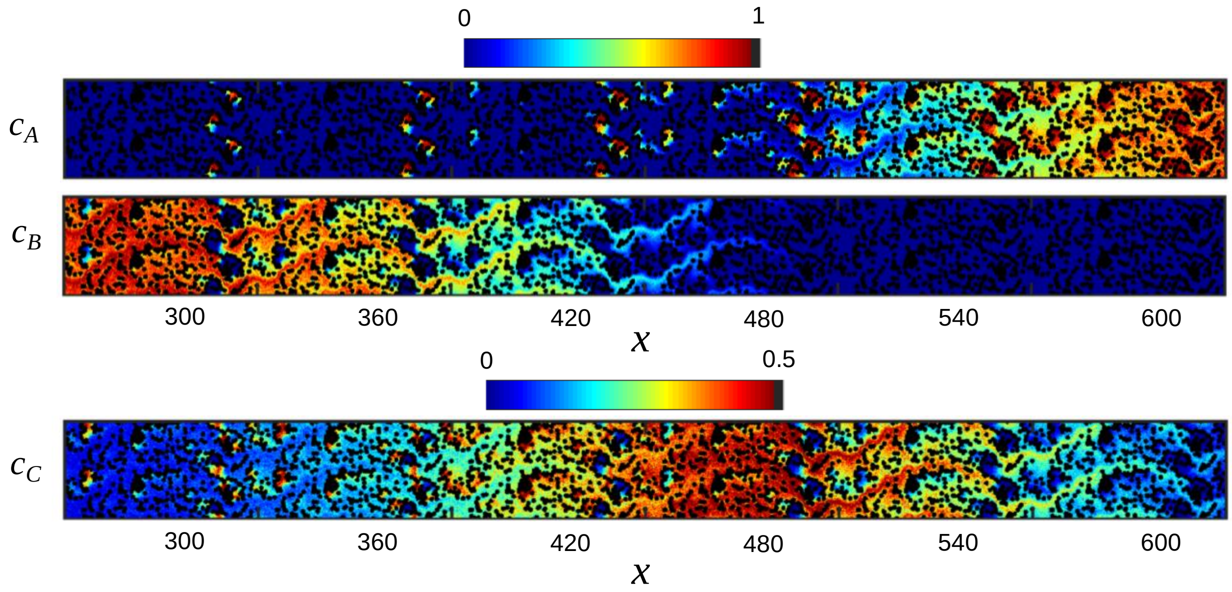

Figure 2. Snapshot of the pore-scale concentration fields c_A, c_B and c_C at time $t = 448$.

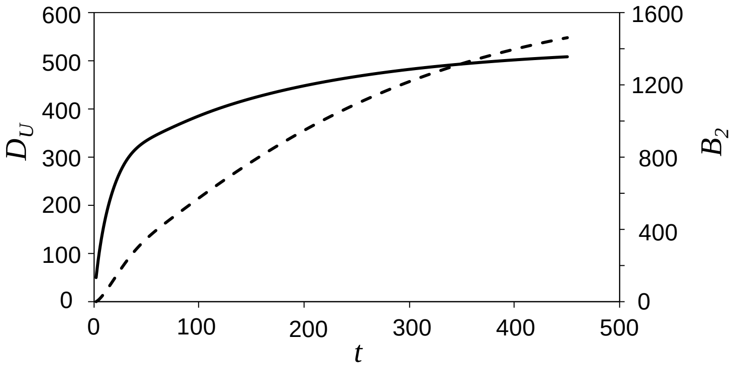

Figure 3. Temporal evolution of the effective dispersion coefficient D_U (16) (continuous curve, left vertical axis) and of B_2 (26) (dashed curve, right vertical axis).

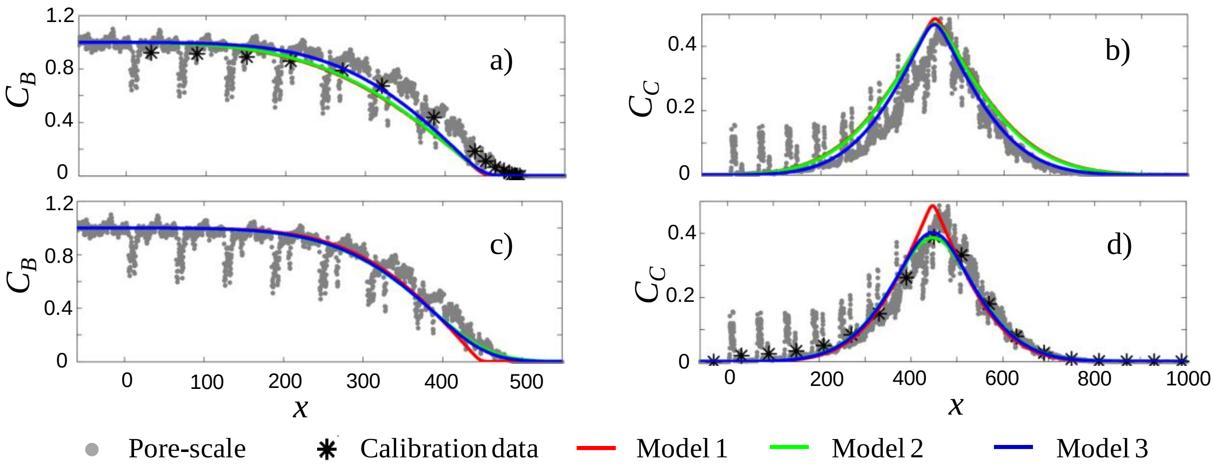

Figure 4. Model calibration results: concentration profiles resulting from model calibration (continuous curves) against data sets $\overline{c}_{Bi}^{*}$ (a-b) and $\overline{c}_{Ci}^{*}$ (c-d); calibration data $\overline{c}_{Bi}^{*}$ (black symbols in a) and $\overline{c}_{Ci}^{*}$ (black symbols in d) and section-averaged concentrations resulting from pore-scale simulations (grey points)

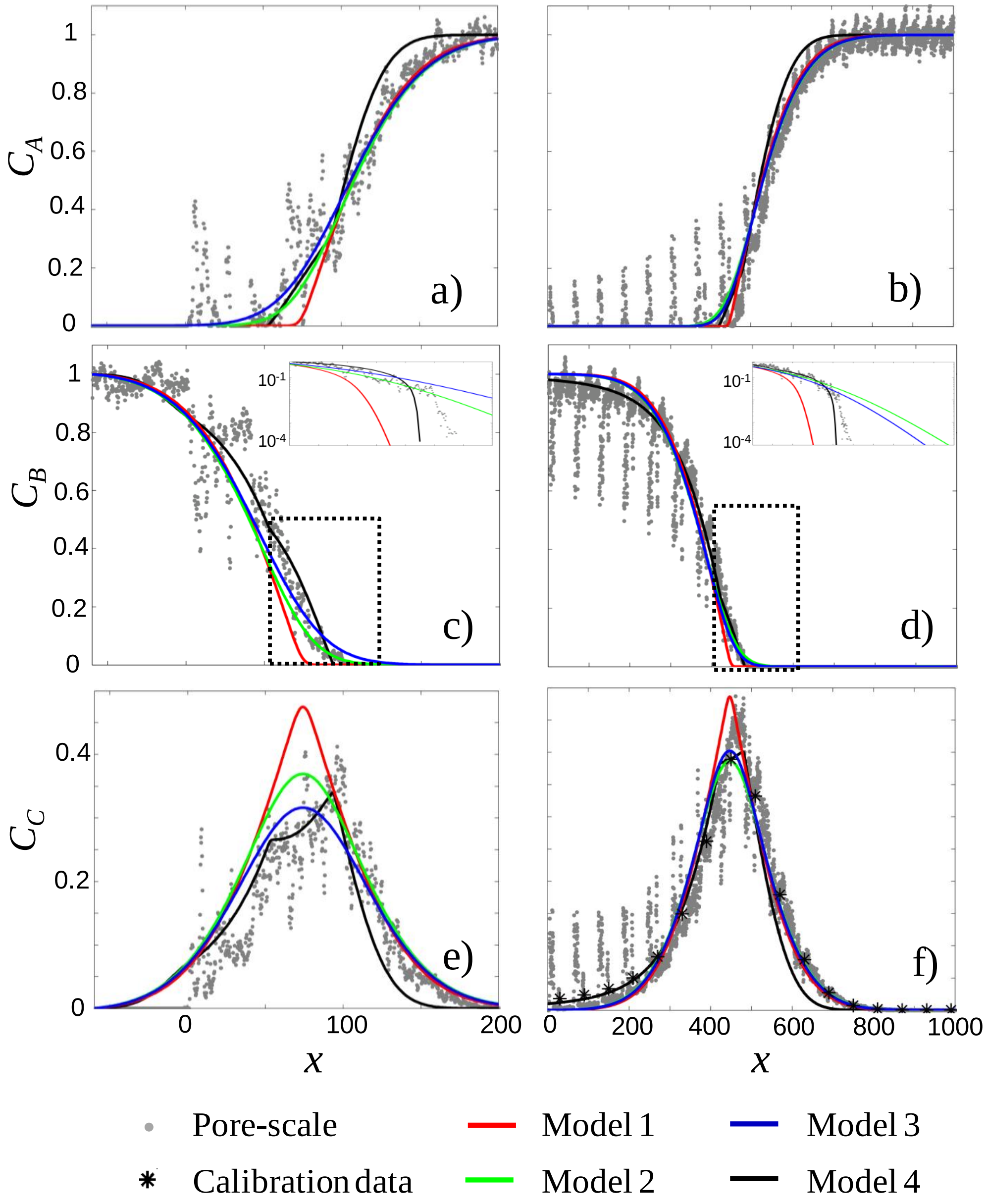

Figure 5. Comparison between section-averaged pore-scale concentrations and continuum-scale model results obtained for reactants A (a-b), B (c-d) and reaction product C (e-f), for dimensionless times t = 47 (left column: a,c,e) and t = 448 (right column: b,d,f). Results of models 1-3 are obtained through model calibration on $\overline{c}_{Ci}^{*}$ data (black symbols in f). Insets in c-d display a zoom (in semi-logarithmic scale) of the regions identified by the dot-dashed boxes.

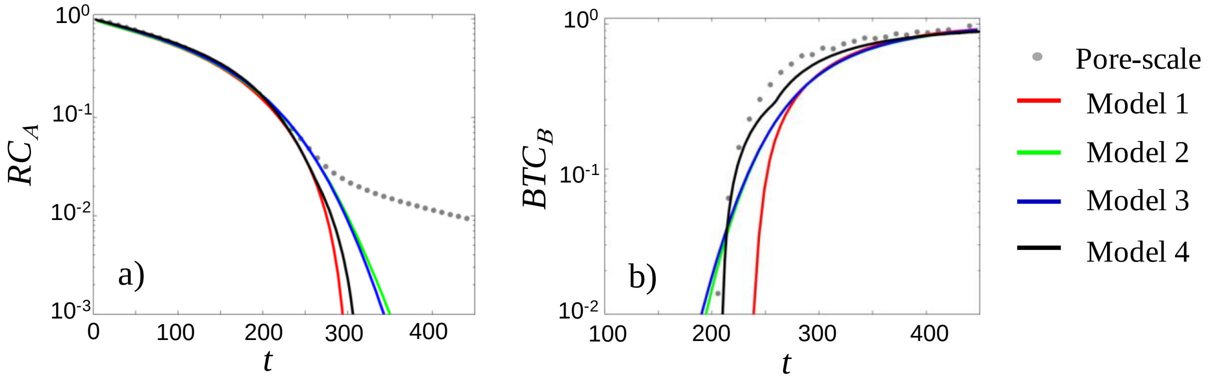

Figure 6. Temporal evolution of (a) flux-weighted concentration of reactant B (BTC_B) at X_M = 300 and (b) residual concentration of species A (RC_A) evaluated with X_M = 300.

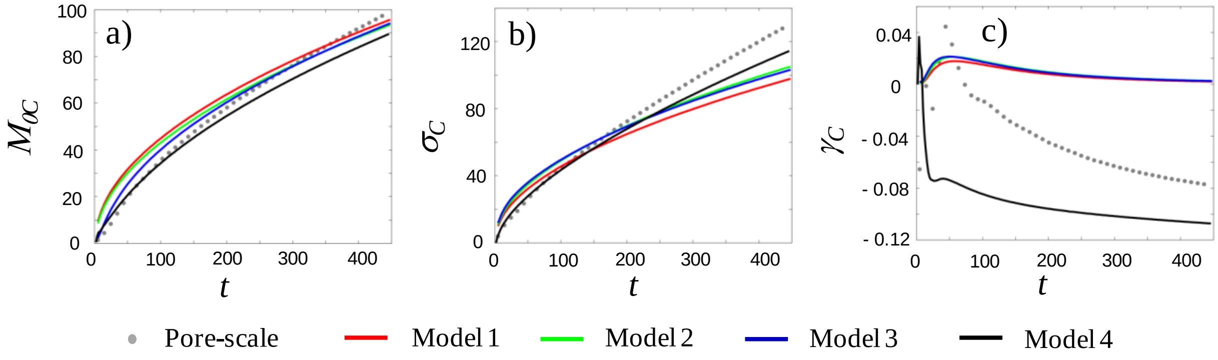

Figure 7. Temporal evolution of (a) the total mass, (b) spreading and (c) skewness associated with the spatial distribution of the reaction product C as given by the considered continuum-scale models (lines) and pore-scale simulation (symbols).